remote sensing

MDPI

Article

Tensor Completion via Smooth Rank Function Low-Rank Approximate Regularization

Shicheng Yu [1], Jiaqing Miao [2,*], Guibing Li [3,4], Weidong Jin [3,5], Gaoping Li [2] and Xiaoguang Liu [2]

[1] School of Big Data and Artificial Intelligence, Chengdu Technological University, Chengdu 611730, China
[2] School of Mathematics, Southwest Minzu University, Chengdu 610041, China
[3] School of Electrical Engineering, Southwest Jiaotong University, Chengdu 611756, China
[4] School of Computer Science and Engineering, Southwest Minzu University, Chengdu 610041, China
[5] China-ASEAN International Joint Laboratory of Integrated Transportation, Nanning University, Nanning 530299, China
* Correspondence: jiaqing_miao@swun.edu.cn; Tel.: +86-177-8067-1494

Abstract: In recent years, the tensor completion algorithm has played a vital part in the reconstruction of missing elements within high-dimensional remote sensing image data. Due to the difficulty of tensor rank computation, scholars have proposed many substitutions of tensor rank. By introducing the smooth rank function (SRF), this paper proposes a new tensor rank nonconvex substitution function that performs adaptive weighting on different singular values to avoid the performance deficiency caused by the equal treatment of all singular values. On this basis, a novel tensor completion model that minimizes the SRF as the objective function is proposed. The proposed model is efficiently solved by adding the hot start method to the alternating direction multiplier method (ADMM) framework. Extensive experiments are carried out in this paper to demonstrate the resilience of the proposed model to missing data. The results illustrate that the proposed model is superior to other advanced models in tensor completeness.

Keywords: hyperspectral image; tensor completion; low-rank; smooth rank function

Citation: Yu, S.; Miao, J.; Li, G.; Jin, W.; Li, G.; Liu, X. Tensor Completion via Smooth Rank Function Low-Rank Approximate Regularization. *Remote Sens.* **2023**, *15*, 3862. https://doi.org/10.3390/rs15153862

Academic Editors: Liang-Jian Deng, Gemine Vivone and Danfeng Hong

Received: 16 May 2023
Revised: 1 August 2023
Accepted: 1 August 2023
Published: 3 August 2023

1. Introduction

Hyperspectral image (HSI) data are obtained by hyperspectral imagers that capture important information regarding the Earth's surface in hundreds of continuous wavebands, and the rich surface structure information they contain are indispensable for identifying objects; as a consequence, HSI data have extensive application prospects and have already played an important role in geological applications, mineral exploration and target detection [1].

Each HSI is naturally represented as a three-dimensional data volume, where one dimension is the spectral direction, and the remaining two dimensions are spatial [2]. In many cases, due to errors or design flaws, the three-dimensional data volume lacks many elements. A specific example of the lack of measurements is snapshot spectral imaging (SSI) [3]. To achieve high temporal resolution imaging, only a small proportion of pixels can be observed in each spectral band. The loss of pixels not only decreases the quality of visual imaging but also adversely impacts the performance of subsequent image analyses, such as target detection and classification [4–6]. The practical application performance based on HSI mainly depends on the efficiency of the algorithm used to recover the missing measurements. Therefore, the efficient and accurate recovery of missing pixels in HSI is currently a highly important research topic.

Tensors or multi-dimensional arrays are widely used in machine vision [7,8], machine learning [9,10], image denoising [11], image reconstruction [12–14] etc. An HSI is a tensor composed of height × width × band number [15] (such as 224 bands). In general, recovering missing pixels in HSI can be formulated as restoring tensors from

corrupted observations (called tensor completion). Due to the high-dimensional nature of HSI, processing and analysis of HSI may encounter storage and computational difficulties. Tensor completion can accurately reconstruct compressed HSI data and improve data access efficiency and processing speed. Therefore, studying tensor completion has important significance for fields that require processing high-dimensional image data, such as geological surveys and crop diagnosis.

Tensor completion is a nondeterministic polynomial hard (NP-hard) inverse problem without prior knowledge. However, in practical applications, the various bands in HSI data are usually highly correlated, so the tensor is essentially determined by the correlation factor of the spectral direction. This structural correlation indicates that it is possible to recover tensors from incomplete or destroyed observation tensor data. At the same time, this prior knowledge mathematically means that the tensor is of low rank, so the tensor completion model usually takes minimizing the tensor rank as the objective function. However, at present, tensor rank has various definitions [16]; commonly used are CANDECOMP/PARAFAC (CP) rank, Tucker rank (also called n rank), and tensor multi-rank. Unfortunately, all tensor ranks are nonconvex, and their calculation is NP hard [17], so obtaining the optimal solution for a tensor completion model is a difficult task. To alleviate this problem, some convex/nonconvex substitution functions are usually used to relax the tensor rank. Liu et al. [7] suggested the tensor trace norm (TTN), which was taken as a convex substitution of the tensor Tucker rank, and proposed the corresponding tensor completion model. TTN needs to unfold the tensor into a series of matrices along each mode, and this simple matricization usually loses the intrinsic spectral direction structure information of HSI. Therefore, the tensor completion method utilizing the inherent structure of HSI is more favored by researchers. To this end, Kilmer et al. [18] constructed the tensor singular value decomposition (t-SVD) framework. On this basis, Semerci et al. [19] defined the tensor nuclear norm (TNN). Zhang et al. [20] used TNN for convex relaxation of tensor multi-rank and video data completion. In addition, Wu et al. [21] proposed a new tensor decomposition method called tensor wheel (TW) decomposition and applied it to tensor completeness.

To promote the performance of tensor completion, various nonconvex surrogate functions have been proposed for tensor rank. Ji et al. [22] and Zhang et al. [23] used the logDet function to perform nonconvex substitution for tensor Tucker rank and proposed a logDet-based tensor completion model. Similarly, Xu et al. [24] used the Laplacian function as a nonconvex alternative to tensor multi-rank. Zhang [25] proposed a nonconvex relaxation method that employs a set of concave functions on the singular values as an approximation of the tensor Tucker rank. Since the approximation effect of the truncated nuclear norm on matrix rank is better than that of the traditional nuclear norm, Xue et al. [26] extended it to the case of tensors and constructed a tensor completion model on this basis. Similarly, since the capped nuclear norm also better approximates the tensor rank, Chen et al. [27] constructed a new completion model using capped nuclear norm regularization and developed a fast solution algorithm based on the majorization minimization [28] framework. Furthermore, Liu et al. [29] and Yang et al. [30] exploited the γ-norm as a nonconvex substitution of tensor multi-rank. Furthermore, Zhao et al. [31] proposed a tensor completion model with a nonconvex tensor rank substitution function, and proved that both the minimax concave penalty function and the smoothly clipped absolute deviation function are equivalent substitutions of the tensor average rank. The above methods are all nonconvex substitutions of tensor rank, which are more effective than TNN and have achieved excellent results in practical applications.

TNN weights all singular values indiscriminately so that the obtained solution may be suboptimal. Many alternatives have been suggested to avoid this limitation. In this paper, a new tensor completion model is constructed that uses the SRF as a low-order relaxation penalty function to approximate the rank function. The SRF can treat different singular values differently through adaptive weight allocation and can also reduce the deviation between the substitution function and the rank function. On this basis, a fast solution

algorithm based on the ADMM [32] is developed. However, the introduction of the SRF leads to nonconvexity of the tensor completion model. Therefore, the hot start method is added to the ADMM framework to assure the convergence of the solution algorithm.

The contributions and advantages of this article are listed below:

(1) This paper uses the SRF as a nonconvex substitution of tensor multi-rank. The SRF can treat different singular values of a tensor differently through adaptive weight allocation, and can approach the rank function more closely than the existing substitution functions. This paper analyzes the convergence of the SRF and proposes a tensor completion model. This provides a new theoretical insight for the study of tensor rank substitution and tensor completion.

(2) A solution algorithm based on the ADMM framework is proposed, and the hot start method is added to assure the convergence of the algorithm, providing technical support for the practical application of the proposed model.

(3) Several experiments are constructed to indicate that the proposed method can restore missing values excellently with greatly compressed data. Therefore, the model proposed in this article can be effectively applied in fields that require processing high-dimensional image data such as geological surveys.

2. Symbols and Preliminary Theory

2.1. Symbol Definitions

In this subsection, the basic symbols are introduced in detail. In this paper, nonbold lowercase letters refer to scalars; bold lowercase letters stand for vectors; bold capital letters represent matrices; bold calligraphic letters refer to tensors. For a third-order tensor $\boldsymbol{\mathcal{Z}}$, the symbols $\boldsymbol{\mathcal{Z}}(i,:,:)$, $\boldsymbol{\mathcal{Z}}(:,j,:)$ and $\boldsymbol{\mathcal{Z}}(:,:,k)$ stand for the horizontal, vertical and front slices of $\boldsymbol{\mathcal{Z}}$, respectively, while $\boldsymbol{\mathcal{Z}}(i,j,:)$, $\boldsymbol{\mathcal{Z}}(i,:,k)$ and $\boldsymbol{\mathcal{Z}}(:,j,k)$ represent the tubes, rows and columns of $\boldsymbol{\mathcal{Z}}$, respectively (see Figure 1). To facilitate writing, $\mathbf{Z}^{(k)}$ refers to the k-th front slice, $z_{ij:}$ stands for $\boldsymbol{\mathcal{Z}}(i,j,:)$, and z_{ijk} represents the (i,j,k)-th element in tensor $\boldsymbol{\mathcal{Z}}$.

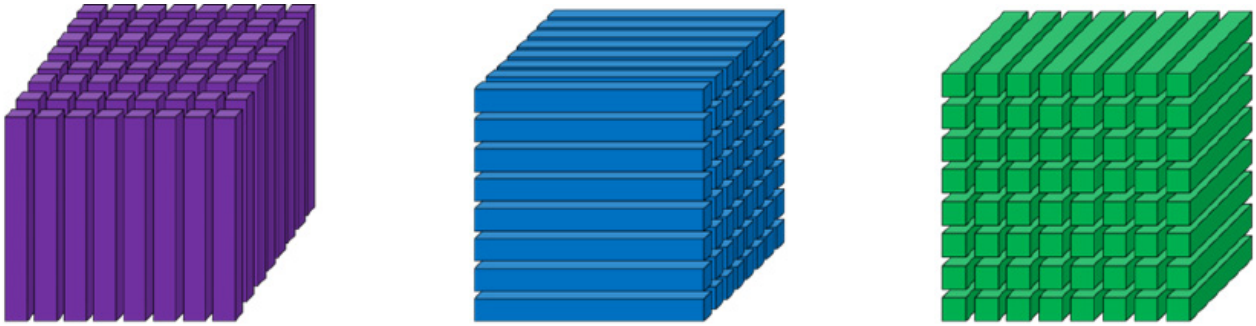

Figure 1. A three-dimensional tensor: (**a**) column fiber; (**b**) row fiber; (**c**) tube fiber.

Definition 1. *(Frobenius norm [18,33]). Suppose* $\boldsymbol{\mathcal{Z}} \in \mathbb{C}^{I_1 \times I_2 \times I_3}$*, the Frobenius norm of* $\boldsymbol{\mathcal{Z}}$ *is* $\|\boldsymbol{\mathcal{Z}}\|_F := \left(\sum_i \sum_j \sum_k \left| z_{ijk} \right|^2 \right)^{\frac{1}{2}}$.

Definition 2. *(third-order t product [18,33]). Suppose* $\boldsymbol{\mathcal{Z}} \in \mathbb{C}^{I_1 \times I_2 \times I_3}$, $\boldsymbol{\mathcal{Y}} \in \mathbb{C}^{I_2 \times I_4 \times I_3}$*, the t-product of* $\boldsymbol{\mathcal{Z}}$ *and* $\boldsymbol{\mathcal{Y}}$ *is a tensor (see Figure 2):*

$$\boldsymbol{\mathcal{X}} := fold(\mathrm{b} - \mathrm{cir}(\boldsymbol{\mathcal{Z}}) unfold(\boldsymbol{\mathcal{Y}})), \tag{1}$$

where $\mathrm{b}-\mathrm{cir}(\boldsymbol{\mathcal{Z}})$ *is called the block circulant matrix, which is defined as:*

$$\mathrm{b}-\mathrm{cir}(\boldsymbol{\mathcal{Z}}) = \begin{bmatrix} \mathbf{Z}^{(1)} & \mathbf{Z}^{(I_3)} & \cdots & \mathbf{Z}^{(2)} \\ \mathbf{Z}^{(2)} & \mathbf{Z}^{(1)} & \cdots & \mathbf{Z}^{(3)} \\ \vdots & \vdots & \ddots & \vdots \\ \mathbf{Z}^{(I_3)} & \mathbf{Z}^{(I_3-1)} & \cdots & \mathbf{Z}^{(1)} \end{bmatrix}. \tag{2}$$

The definitions of the expansion operator $\mathrm{unfold}(\cdot)$ *and its inverse operator* $\mathrm{fold}(\cdot)$ *are as follows:*

$$\mathrm{unfold}(\boldsymbol{\mathcal{Y}}) := \begin{bmatrix} \mathbf{Y}^{(1)} \\ \mathbf{Y}^{(2)} \\ \vdots \\ \mathbf{Y}^{(I_3)} \end{bmatrix}, \ \mathrm{fold}(\mathrm{unfold}(\boldsymbol{\mathcal{Y}})) = \boldsymbol{\mathcal{Y}}. \tag{3}$$

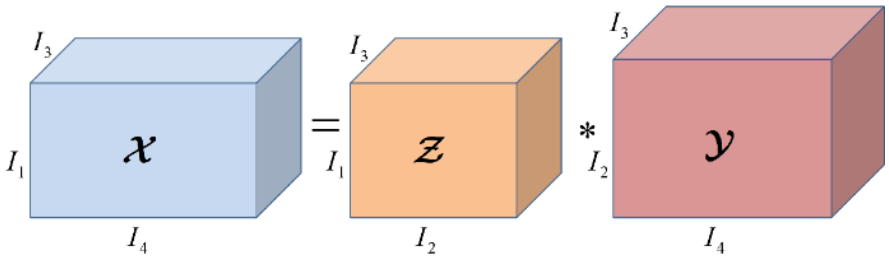

Figure 2. The t-product of $\boldsymbol{\mathcal{Z}}$ and $\boldsymbol{\mathcal{Y}}$.

We can consider a tensor $\boldsymbol{\mathcal{Z}} \in \mathbb{C}^{I_1 \times I_2 \times I_3}$ as an $I_1 \times I_2$ matrix, each component of which is a tube. Therefore, when $I_3 = 1$, the t-product is simplified as the matrix product.

Definition 3. *(third-order tensor conjugate transpose [18,33]). Given* $\boldsymbol{\mathcal{Z}} \in \mathbb{C}^{I_1 \times I_2 \times I_3}$*, the size of the transpose tensor* $\boldsymbol{\mathcal{Z}}^H \in \mathbb{C}^{I_2 \times I_1 \times I_3}$ *is* $I_2 \times I_1 \times I_3$*, which is obtained by transposing each front slice (see Figure 3).*

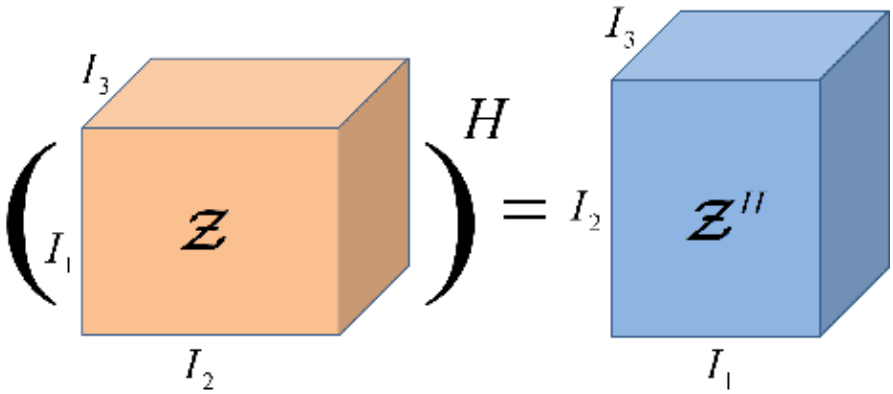

Figure 3. The transpose tensor.

Definition 4. *(third-order identity tensor [18,33]). The identity tensor* $\boldsymbol{\mathcal{E}} \in \mathbb{C}^{I_1 \times I_1 \times I_3}$ *is shown in Figure 4, in which the elements in the grid are 1 and the rest are 0; that is, the first front slice of the tensor* $\boldsymbol{\mathcal{E}}$ *is a unit matrix, while the remaining front slices are all zero matrices.*

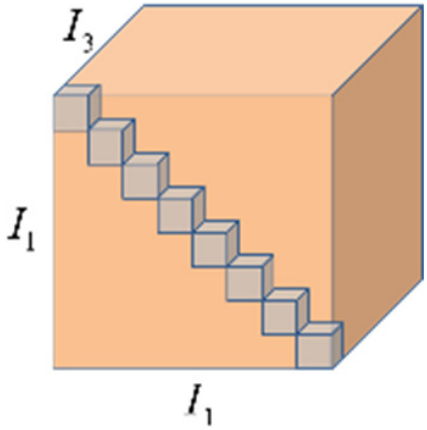

Figure 4. The identity tensor $\boldsymbol{\mathcal{E}} \in \mathbb{C}^{I_1 \times I_1 \times I_3}$.

Definition 5. *(f-diagonal third-order tensor [18,33]). All front slices of the f-diagonal tensor are diagonal matrices (see Figure 5).*

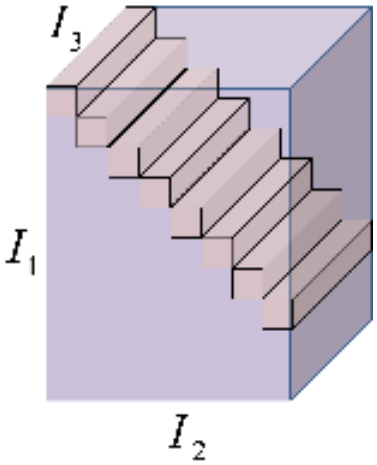

Figure 5. The *f*-diagonal tensor.

Definition 6. *(orthogonal third-order tensor [18,33]). If the tensor data* $\boldsymbol{\mathcal{U}} \in \mathbb{C}^{I_1 \times I_1 \times I_3}$ *satisfy* $\boldsymbol{\mathcal{U}} * \boldsymbol{\mathcal{U}}^H = \boldsymbol{\mathcal{U}}^H * \boldsymbol{\mathcal{U}} = \boldsymbol{\mathcal{E}}$*, where* $\boldsymbol{\mathcal{E}}$ *is an identity tensor, then* $\boldsymbol{\mathcal{U}}$ *is named an orthogonal third-order tensor.*

Definition 7. *(t-SVD [33]). A tensor* $\boldsymbol{\mathcal{Z}} \in \mathbb{C}^{I_1 \times I_2 \times I_3}$ *can be expressed as* $\boldsymbol{\mathcal{Z}} = \boldsymbol{\mathcal{U}} * \boldsymbol{\mathcal{S}} * \boldsymbol{\mathcal{V}}^H$ *(see Figure 6), where* $\boldsymbol{\mathcal{S}} \in \mathbb{C}^{I_1 \times I_2 \times I_3}$ *is the f-diagonal tensor,* $\boldsymbol{\mathcal{U}} \in \mathbb{C}^{I_1 \times I_1 \times I_3}$ *and* $\boldsymbol{\mathcal{V}} \in \mathbb{C}^{I_2 \times I_2 \times I_3}$ *are orthogonal third-order tensors.*

In t-SVD, the Fourier transform is performed in the direction of the tube first, and $\widetilde{\boldsymbol{\mathcal{Z}}} = \mathrm{dft}(\boldsymbol{\mathcal{Z}}, [], 3)$ is used to represent the discrete Fourier transform (DFT) along each tube of the tensor $\boldsymbol{\mathcal{Z}}$. Second, in the SVD framework, matrix factorization is performed for each front slice of $\widetilde{\boldsymbol{\mathcal{Z}}}$ to obtain matrices $\widetilde{\boldsymbol{U}}^{(j)}$, $\widetilde{\boldsymbol{S}}^{(j)}$, $\left(\widetilde{\boldsymbol{V}}^{(j)}\right)^H$, $j = 1, \cdots, I_3$. Third, $\widetilde{\boldsymbol{U}}^{(j)}$, $\widetilde{\boldsymbol{S}}^{(j)}$ and $\left(\widetilde{\boldsymbol{V}}^{(j)}\right)^H$ are used as front slices to form tensors $\widetilde{\boldsymbol{\mathcal{U}}}$, $\widetilde{\boldsymbol{\mathcal{S}}}$ and $\widetilde{\boldsymbol{\mathcal{V}}}^H$, respectively. Finally, the inverse Fourier transform is performed along the tube direction of tensors $\widetilde{\boldsymbol{\mathcal{U}}}$, $\widetilde{\boldsymbol{\mathcal{S}}}$ and $\widetilde{\boldsymbol{\mathcal{V}}}^H$ to obtain $\boldsymbol{\mathcal{U}}$, $\boldsymbol{\mathcal{S}}$ and $\boldsymbol{\mathcal{V}}^H$.

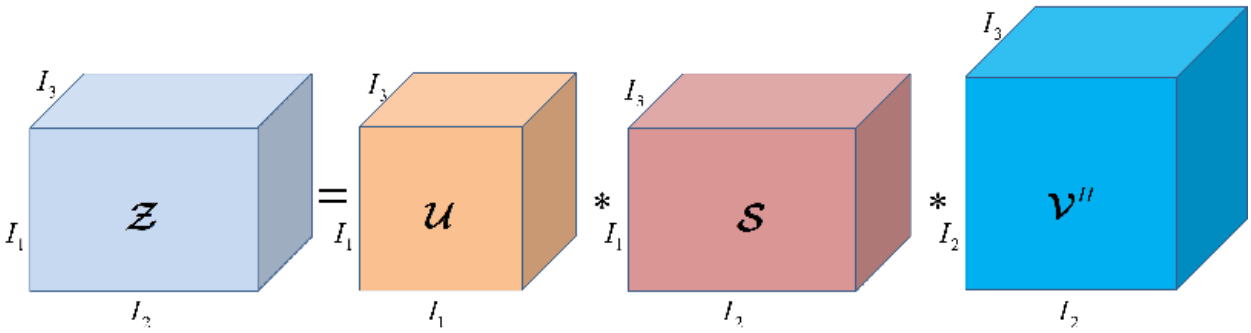

Figure 6. The t-SVD result of $\mathcal{Z}$.

2.2. Preliminary Theory

The low-rank structure is the basic and powerful prior information of a tensor and is widely used in tensor completion algorithms [34–36]. Mathematically, the specific tensor completion model is:

$$\begin{array}{c} \underset{\mathcal{Z}}{\operatorname{argmin}} \operatorname{rank}(\mathcal{Z}) \\ \text{s.t. } \mathcal{Z}_\Omega = \mathcal{B}_\Omega \end{array}, \tag{4}$$

where $*_\Omega$ represents the element corresponding to the $*$ tensor in the index set Ω, the remaining items are set to zero, and $\mathcal{B}$ represents the observed tensor.

At present, tensor rank includes CP-rank [37], Tucker rank [38], tensor multi-rank [33], etc. The definition of CP rank is straightforward, but its calculation is an NP-hard problem [39], which greatly limits CP rank in tensor completion. The Tucker rank of $\mathcal{Z} \in \mathbb{C}^{I_1 \times I_2 \times \cdots \times I_n}$ is represented by $\operatorname{rank}_{\text{tc}}(\mathcal{Z})$, and its definition is as follows:

$$\operatorname{rank}_{\text{tc}}(\mathcal{Z}) := \Big(\operatorname{rank}(\mathbf{Z}_{(1)}), \ldots, \operatorname{rank}(\mathbf{Z}_{(n)})\Big), \tag{5}$$

with $\mathbf{Z}_{(j)}$ denoting the j-th mode unfolding matrix of tensor $\mathcal{Z}$. By definition, $\operatorname{rank}_{\text{tc}}(\mathcal{Z})$ is obtained by the matrix rank, so it is easy to calculate. Usually, the weighted sum of each component of $\operatorname{rank}_{\text{tc}}(\mathcal{Z})$ is penalized to minimize it; that is, the following formula is used as the objective function of the tensor completion model:

$$S(\mathcal{Z}) = \sum_{j=1}^{n} w_j \operatorname{rank}(\mathbf{Z}_{(j)}), \tag{6}$$

where $w_j \geq 0$ is the weight and $\sum_{j=1}^{n} w_j = 1$.

The tensor completion model with Equation (6) as the objective function is an NP-hard problem. To solve it effectively, TTN [7] is usually used as a convex surrogate for Equation (6). Notably, the Tucker rank may not be a good representation of the tensor rank because the expansion of tensors according to the mode-unfolding operator destroys the characteristic structure of tensors, especially in the case of hyperspectral tensor image data, because the unfolding operator seriously damages the structure of the spectrum direction. Even with TTN convex substitution, the disadvantage of the tensor's characteristic structure being destroyed cannot be effectively avoided.

To avoid the destruction of the tensor's characteristic structure, tensor multi-rank is proposed. The multi-rank of $\mathcal{Z} \in \mathbb{C}^{I_1 \times I_2 \times I_3}$ takes the rank of $\widetilde{\mathcal{Z}}^{(j)}$ as a vector of its j-th element. TNN [19,20] is usually used as a substitution for multi-rank. Given tensor $\mathcal{Z} \in \mathbb{C}^{I_1 \times I_2 \times I_3}$, the TNN of $\mathcal{Z}$ is:

$$\|\mathcal{Z}\|_* := \frac{1}{I_3} \sum_{k=1}^{I_3} \left\|\widetilde{\mathcal{Z}}^{(k)}\right\|_*, \tag{7}$$

where $\|\cdot\|_*$ represents the nuclear norm. Taking the TNN as the objective function, the following important tensor completion model is obtained:

$$\begin{array}{l} \underset{\mathcal{Z}}{\operatorname{argmin}} \ \|\mathcal{Z}\|_* \\ \text{s.t. } \mathcal{Z}_\Omega = \mathcal{B}_\Omega \end{array}, \tag{8}$$

TNN treats each singular value of a tensor equally and assigns them the same weight, which greatly limits the tensor complete performance and the flexibility of TNN to deal with practical problems. This is because the singular values of the tensor have specific physical meanings, and different singular values should be assigned different weights. Therefore, it is difficult to accurately restore the missing values using the TNN-based model (8).

3. Proposed Method

In this section, the rank function is replaced by the SRF under the DFT. On this basis, a new tensor completion model is established. In addition, the corresponding solution method is proposed according to the ADMM framework.

3.1. Tensor Completion Model Based on Smooth Rank Function

To treat singular values differently through adaptive weight allocation and reduce the deviation between the substitution and rank function, this paper will replace the multi-rank function with the nonconvex SRF regularization term.

The SRF is defined as $1 - e^{-x^2/\delta^2}$ [40], which is closer to the l_0 pseudonorm (see Figure 7). That is, when solving the rank minimization problem, the SRF function approximates the multi-rank function better than the existing substitutions. Furthermore, in the TNN, all singular values of each front slice are assigned a weight of $\frac{1}{I_3}$. However, for hyperspectral remote sensing images, singular values have different degrees of significance, so different weights should be assigned to them [41]. For example, a smaller singular value represents high-frequency information and noise, whereas a larger singular value represents low-frequency information. SRF can automatically assign different weights to each singular value. Based on the above two points, given $\mathcal{Z} \in \mathbb{C}^{I_1 \times I_2 \times I_3}$, the following nonconvex substitution based on SRF to the multi-rank function is proposed:

$$\mathcal{G}_\delta(\mathcal{Z}) = \sum_{j=1}^{I_3} \sum_{k=1}^{\ell} \left(1 - e^{-\sigma_k^2(\widetilde{\mathbf{Z}}^{(j)})/\delta^2}\right), \tag{9}$$

where $\ell = \min\{I_1, I_2\}$, $\sigma_k(*)$ refers to the k-th singular value of $*$, and the parameter $\delta > 0$ is small. To avoid falling into local minima and to ensure the convergence of the solution framework for the tensor completion model (10) that will be proposed below, the initial value of δ is set to a large value at the beginning of the iteration. With increasing iterations, the δ value decreases gradually. Incorporating Equation (9) into Equation (4), the following model that can efficaciously recover the missing elements in HSI data is proposed:

$$\begin{array}{l} \underset{\mathcal{Z}}{\operatorname{argmin}} \ \mathcal{G}_\delta(\mathcal{Z}) \\ s.t. \ \mathcal{Z}_\Omega = \mathcal{B}_\Omega \end{array}. \tag{10}$$

3.2. Convergence Analysis of the Smooth Rank Function

The SRF is a pseudo norm, but it has some nice properties. According to these properties, a solution algorithm for the tensor completion model (10) is proposed in this paper.

Lemma 1. $\lim_{\delta \to 0} \mathcal{G}_\delta(\mathcal{Z}) = \left(rank\left(\widetilde{\mathbf{Z}}^{(1)}\right), \cdots, rank\left(\widetilde{\mathbf{Z}}^{(I_3)}\right)\right)$.

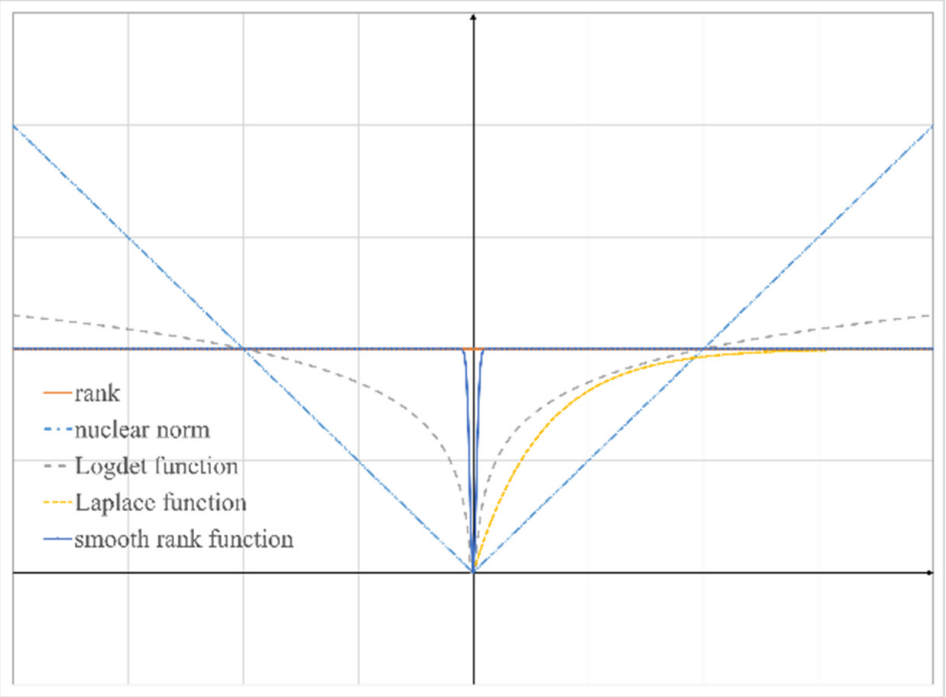

Figure 7. Graph of the low-rank function, nuclear norm, LogDet function, Laplace function and SRF of scalars.

Proof of Lemma 1. First, consider the case of a single slice; for the j-th front slice, $\boldsymbol{G}_\delta\left(\widetilde{\boldsymbol{Z}}^{(j)}\right) = \sum_{k=1}^{\ell}\left(1 - e^{-\sigma_k^2(\widetilde{\boldsymbol{Z}}^{(j)})/\delta^2}\right)$. When δ becomes infinitely small,

$$1 - e^{-\sigma_k^2(\widetilde{\boldsymbol{Z}}^{(j)})/\delta^2} \to \begin{cases} 0, & if\ \sigma_k\left(\widetilde{\boldsymbol{Z}}^{(j)}\right) = 0 \\ 1, & if\ \sigma_k\left(\widetilde{\boldsymbol{Z}}^{(j)}\right) > 0 \end{cases}. \tag{11}$$

Therefore, when $\delta \to 0$, $\boldsymbol{G}_\delta\left(\widetilde{\boldsymbol{Z}}^{(j)}\right)$ tends to the zero-norm of vector $\left(\sigma_1(\widetilde{\boldsymbol{Z}}^{(j)}), \cdots, \sigma_l(\widetilde{\boldsymbol{Z}}^{(j)})\right)$, that is,

$$\lim_{\delta \to 0} \boldsymbol{G}_\delta\left(\widetilde{\boldsymbol{Z}}^{(j)}\right) = rank\left(\widetilde{\boldsymbol{Z}}^{(j)}\right). \tag{12}$$

Equation (12) is satisfied for each slice, so the lemma is proven. □

Theorem 1. *Given $\boldsymbol{\mathcal{Y}} \in \mathbb{C}^{I_1 \times I_2 \times I_3}$, suppose there is the following minimization function:*

$$\min_{\boldsymbol{\mathcal{Z}}} \ \boldsymbol{\mathcal{G}}_\delta(\boldsymbol{\mathcal{Z}}) + \frac{\beta}{2}\|\boldsymbol{\mathcal{Z}} - \boldsymbol{\mathcal{Y}}\|_F^2. \tag{13}$$

According to the generalized weighted singular value threshold method (WSVT) used in [42], the optimal solution of Equation (13) is $\boldsymbol{\mathcal{Z}}^* = \boldsymbol{\mathcal{U}} * \boldsymbol{\mathcal{D}}_{\frac{\nabla\phi}{\beta}} * \boldsymbol{\mathcal{V}}^H$, where $\boldsymbol{\mathcal{U}}$ and $\boldsymbol{\mathcal{V}}^H$ are obtained by t-SVD of $\boldsymbol{\mathcal{Y}}$, that is, $\boldsymbol{\mathcal{Y}} = \boldsymbol{\mathcal{U}} * \boldsymbol{\mathcal{S}} * \boldsymbol{\mathcal{V}}^H$. $\boldsymbol{\mathcal{D}}_{\frac{\nabla\phi}{\beta}} \in \mathbb{C}^{I_1 \times I_2 \times I_3}$ is an f-diagonal third-order tensor, the element on the catercorner of each front slice of $\widetilde{\boldsymbol{\mathcal{D}}}_{\frac{\nabla\phi}{\beta}}$ is $\widetilde{\boldsymbol{\mathcal{D}}}_{\frac{\nabla\phi}{\beta}}(k,k,j) = (\widetilde{\boldsymbol{\mathcal{S}}}(k,k,j) - \frac{\nabla\phi(\sigma_k^j)}{\beta})_+, j = 1, \cdots, I_3$. $\nabla\phi(\sigma_k^j)$ is the gradient of function $\phi = 1 - e^{-\sigma_k^2(\widetilde{\boldsymbol{Z}}^{(j)})/\delta^2}$ at σ_k^j, and σ_k^j stands for the k-th singular value of $\widetilde{\boldsymbol{Z}}^{(j)}$.

Proof of Theorem 1. Because the expression of the SRF is $\mathcal{G}_\delta(\mathcal{Z}) = \sum_{j=1}^{I_3}\sum_{k=1}^{\ell}\left(1 - e^{-\sigma_k^2(\widetilde{\mathcal{Z}}^{(j)})/\delta^2}\right)$, Equation (13) can be reformulated as:

$$\min \sum_{j=1}^{I_3}\left(\sum_{k=1}^{\ell}\left(1 - e^{-\sigma_k^2(\widetilde{\mathcal{Z}}^{(j)})/\delta^2}\right) + \frac{\beta}{2}\left\|\widetilde{\mathcal{Z}}^{(j)} - \widetilde{\mathcal{Y}}^{(j)}\right\|_F^2\right). \tag{14}$$

Since

$$\phi(\sigma_k^j) \approx \nabla\phi(\sigma_k^j)\left(\sigma_k^j - 0\right) + \phi(0) = \nabla\phi(\sigma_k^j)\sigma_k^j, \tag{15}$$

according to WSVT, for any $j = 1, \cdots, I_3$, the solution that minimizes $\sum_{k=1}^{\ell}\left(1 - e^{-\sigma_k^2(\widetilde{\mathcal{Z}}^{(j)})/\delta^2}\right) + \frac{\beta}{2}\left\|\widetilde{\mathcal{Z}}^{(j)} - \widetilde{\mathcal{Y}}^{(j)}\right\|_F^2$ is:

$$\widetilde{\mathcal{Z}}^{(j)*} = \widetilde{\mathcal{U}}^{(j)} * \widetilde{\mathcal{D}}^{(j)}_{\frac{\nabla\phi}{\beta}} * \left(\widetilde{\mathcal{V}}^{(j)}\right)^H, \tag{16}$$

where $\widetilde{\mathcal{Y}}^{(j)} = \widetilde{\mathcal{U}}^{(j)} * \widetilde{\mathcal{S}}^{(j)} * \left(\widetilde{\mathcal{V}}^{(j)}\right)^H$, and $\widetilde{\mathcal{D}}^{(j)}_{\frac{\nabla\phi}{\beta}} = \mathrm{Diag}\left\{\left(\widetilde{\mathcal{S}}^{(j)}(k,k) - \frac{\nabla\phi(\sigma_k^j)}{\beta}\right)_+\right\}$. Therefore, the theorem is proven. □

3.3. Solution Algorithm

In this subsection, based on the ADMM framework and Theorem 1, a method for solving the tensor completion model (10) is developed. First, we introduce the following function:

$$l_{\mathbb{S}}(\mathcal{Z}) = \begin{cases} 0, & \text{if } \mathcal{Z} \in \mathbb{S} \\ \infty, & \text{otherwise} \end{cases}, \tag{17}$$

where $\mathbb{S} := \left\{\mathcal{Z} \in \mathbb{R}^{I_1 \times I_2 \times I_3}, \mathcal{Z}_\Omega = \mathcal{B}_\Omega\right\}$, and Equation (10) can be reformulated as

$$\min_{\mathcal{Z}} \ \mathcal{G}_\delta(\mathcal{Z}) + l_{\mathbb{S}}(\mathcal{Z}). \tag{18}$$

Then, the variable $\mathcal{Y} = \mathcal{Z}$ is introduced, and the following augmented Lagrangian function of Equation (18) is obtained:

$$\begin{aligned} L(\mathcal{Z}, \mathcal{Y}, \mathcal{W}) &:= \mathcal{G}_\delta(\mathcal{Z}) + \mathbf{1}_{\mathbb{S}}(\mathcal{Y}) + \langle \mathcal{Y} - \mathcal{Z}, \mathcal{W}\rangle + \frac{\beta}{2}\|\mathcal{Y} - \mathcal{Z}\|_F^2 \\ &= \mathcal{G}_\delta(\mathcal{Z}) + \mathbf{1}_{\mathbb{S}}(\mathcal{Y}) + \frac{\beta}{2}\left\|\mathcal{Y} - \mathcal{Z} + \frac{1}{\beta}\mathcal{W}\right\|_F^2 + c \end{aligned}, \tag{19}$$

where $\mathcal{W} \in \mathbb{R}^{I_1 \times I_2 \times I_3}$ is the Lagrangian multiplier, c is a constant dependent on $\mathcal{W}$, and β is a regularization balance parameter. According to the ADMM framework, $\mathcal{Z}$, $\mathcal{Y}$ and $\mathcal{W}$ can be updated iteratively as:

$$\begin{cases} \mathcal{Z}^{l+1} = \underset{\mathcal{Z}}{\mathrm{argmin}} L(\mathcal{Z}, \mathcal{Y}^l, \mathcal{W}^l) \\ \mathcal{Y}^{l+1} = \underset{\mathcal{Y}}{\mathrm{argmin}} L(\mathcal{Z}^{l+1}, \mathcal{Y}, \mathcal{W}^l), \\ \mathcal{W}^{l+1} = \mathcal{W}^l + \alpha(\mathcal{Y}^{l+1} - \mathcal{Z}^{l+1}) \end{cases} \tag{20}$$

where α represents the step size. According to the ADMM, Equation (20) can be decomposed into three subproblems as follows:

$$\begin{cases} \min\limits_{\mathcal{Z}} \mathcal{G}_\delta(\mathcal{Z}) + \frac{\beta}{2}\left\|\mathcal{Z} - \mathcal{Y}^l - \frac{1}{\beta}\mathcal{W}^l\right\|_F^2 & \text{(a)} \\ \min\limits_{\mathcal{Y}} l_{\mathbb{S}}(\mathcal{Y}) + \frac{\beta}{2}\left\|\mathcal{Z}^{l+1} - \mathcal{Y} - \frac{1}{\beta}\mathcal{W}^l\right\|_F^2 & \text{(b)} \\ \mathcal{W}^{l+1} = \mathcal{W}^l + \alpha(\mathcal{Y}^{l+1} - \mathcal{Z}^{l+1}) & \text{(c)} \end{cases}. \tag{21}$$

The specific steps to solve the first two subproblems are given below.

First, solve subproblem (21a). From Theorem 1, the optimal solution for (21a) is:

$$\mathcal{Z}^{l+1} = \mathcal{U}^l * \mathcal{D}^l_{\frac{\nabla\phi}{\beta}} * \left(\mathcal{V}^l\right)^H, \tag{22}$$

where $\mathcal{X}^l = \mathcal{U}^l * \mathcal{S}^l * \left(\mathcal{V}^l\right)^H$ is the t-SVD of $\mathcal{X}^l = \mathcal{Y}^l + \frac{1}{\beta}\mathcal{W}^l$, $\mathcal{D}^l_{\frac{\nabla\phi}{\beta}} \in \mathbb{C}^{I_1 \times I_2 \times I_3}$ is an f-diagonal third-order tensor, the element on the diagonal of each front slice of $\widetilde{\mathcal{D}}^l_{\frac{\nabla\phi}{\beta}}$ is $\widetilde{\mathcal{D}}^l_{\frac{\nabla\phi}{\beta}}(k,k,j) = (\widetilde{\mathcal{S}}^l(k,k,j) - \frac{\nabla\phi^l(\sigma_k^j)}{\beta})_+$, $j = 1, \cdots, I_3$, and $\nabla\phi^l(\sigma_k^j)$ is the gradient of function $\phi^l = 1 - e^{-\sigma_k^2((\widetilde{\mathcal{Z}}^l)^{(j)})/\delta^2}$ at $\sigma_k\left(\left(\widetilde{\mathcal{Z}}^l\right)^{(j)}\right)$.

Second, solve subproblem (21b). Obviously, the objective function of (21b) is differentiable, so the solution of (21b) is:

$$\mathcal{Y}^{l+1} = (\mathcal{Z}^{l+1} - \frac{1}{\beta}\mathcal{W}^l)_{\Omega^c} + \mathcal{B}, \tag{23}$$

with Ω^c referring to the complement of Ω.

The complete steps of the ADMM-based solution algorithm for the proposed model are summarized in Algorithm 1.

Algorithm 1. The ADMM-based algorithm for solving the model (10).

Input:
Observed data $\mathcal{B}$, index set Ω, parameters α, β and δ^2;
Enter the maximum number of iterations $L_{\max} = 500$, tol$= 10^{-6}$, let $\mathcal{Z}^0 = \mathcal{B}$, $\mathcal{Y}^0 = \mathbf{0}$, $\mathcal{W}^0 = \mathbf{0}$;
for $l = 1$ to $L_{\max}$:
Let $\mathcal{X}^l = \mathcal{Y}^l + \frac{1}{\beta}\mathcal{W}^l$;
$\mathcal{U}^l, \mathcal{S}^l, \left(\mathcal{V}^l\right)^H$ is obtained by performing t-SVD on $\mathcal{X}^l$;
Update $\mathcal{Z}^{l+1}$ on the grounds of formula (22);
Update $\mathcal{Y}^{l+1}$ on the grounds of formula (23);
Update $\mathcal{W}^{l+1}$ on the grounds of formula (21c);
If $\left\|\mathcal{Z}^{l+1} - \mathcal{Z}^l\right\|_F / \left\|\mathcal{Z}^l\right\|_F < tol$, terminate loop;
end for
return $\mathcal{Z}$;
Output:
The recovered tensor $\mathcal{Z}$.

4. Experiment

4.1. Data and Experimental Environment

For this article, we conducted five sets of experiments on three sets of HSI data synthesized through the hyperspectral library, a distribution map of ground object types from the Remote Sensing Imaging Processing Center of the National University of Singapore, and the well-known AVIRIS Cuprite dataset. For these experiments, to synthesize the HSI data, two different spectral databases were considered: $A_1 \in \mathbb{R}^{100\times120}$ and $A_2 \in \mathbb{R}^{224\times240}$. A_1 is a subset generated from the NASA Johnson Space Center (NASA-JSC) spectral characteristics database, which includes 262 end members with 100 bands [43]. This spectral

database has been widely used in HSI analysis. $\boldsymbol{A}_2$ is a random selection of 240 elements from the USGS Digital Spectrum Database (splib06a) [44]. This spectral database contains 224 bands uniformly distributed within 0.4–2.5 µm. This spectral database is widely used in hyperspectral unmixing.

The simulation dataset 1 (DS1) used in example 1 is generated from nine end members randomly selected from the spectral database $\boldsymbol{A}_1$. The data contain 100 × 100 pixels and 100 bands. The simulation dataset 2 (DS2) in example 2 is generated by randomly selecting four end members in the spectral database $\boldsymbol{A}_2$. The data contain 100 × 100 pixels, and each pixel contains 224 bands. The simulation dataset 3 (DS3) in example 3 is generated by randomly selecting five end members from the spectral database $\boldsymbol{A}_2$. The data contain 75 × 75 pixels, and each pixel contains 100 bands. In example 4, the data are a distribution map of ground object types from the Remote Sensing Imaging Processing Center of the National University of Singapore. The data contain 278 × 329 pixels. The data in Example 5 are from the AVIRIS Cuprite dataset, which is a mineral map drawn by the U.S. Geological Survey in 1995 and contains 224 spectral bands, ranging from 0.4–2.5 µm. The experiment uses a data subset of 350 × 350 pixels, and the spectral bands are reduced to 188 after removing the water absorption band and data with a low signal-to-noise ratio. The relevant information of the data is summarized in Table 1.

Table 1. The relevant information of the data in 5 experiments.

	Data Source	**Data Size (Height × Width × Band)**
Example 1	Generated from nine end members randomly selected from the subset $\boldsymbol{A}_1$ generated from the NASA Johnson Space Center (NASA-JSC) spectral characteristics database	100 × 100 × 100
Example 2	Generated from four end members randomly selected from $\boldsymbol{A}_2$ generated from the United States Geological Survey (USGS) digital spectrum database	100 × 100 × 224
Example 3	Generated by randomly selecting five end members from $\boldsymbol{A}_2$	75 × 75 × 100
Example 4	Distribution map of ground object types from the Remote Sensing Imaging Processing Center of the National University of Singapore	278 × 329 × 100
Example 5	The AVIRIS Cuprite dataset	350 × 350 × 188

All experimental codes were written in MATLAB (R2020a) and executed on a computer with an Intel Core i7-7700K processor (4.20 GHz) and 16 GB of RAM.

4.2. Experimental Results

In the following, the proposed tensor completion method is contrasted with the existing methods, such as HaLRTC [7], TNN, logDet-based method (denoted as LogDet-TC) and Laplace-based method (denoted as Laplace-TC). The peak signal-to-noise ratio (PSNR) and structural similarity (SSIM) values are used to measure the performance of various

algorithms. Suppose $\boldsymbol{F}_o$ is the original monochrome image, and $\boldsymbol{F}_r$ is the corresponding reconstructed image. Then PSNR is defined as:

$$PSNR = 10 \cdot \log_{10} \left(\frac{MAX_{\boldsymbol{F}_o}^2}{\frac{1}{I_1 \times I_2} \sum_{i=1}^{I_1} \sum_{j=1}^{I_2} [\boldsymbol{F}_o(i,j) - \boldsymbol{F}_r(i,j)]^2} \right), \tag{24}$$

where I_1 and I_2 are the height and width of the image, $MAX_{\boldsymbol{F}_o}$ is the maximum value of pixels on the image, and $\frac{1}{I_1 \times I_2} \sum_{i=1}^{I_1} \sum_{j=1}^{I_2} [\boldsymbol{F}_o(i,j) - \boldsymbol{F}_r(i,j)]^2$ is the mean squared error (MSE). For HSI data, the definition of PSNR is similar, but the MSE is the sum of the squares of all differences divided by the image size and then divided by the number of bands. The larger the PSNR, the better the quality of the image reconstruction.

In addition, SSIM is defined as:

$$SSIM = \frac{(2\mu_{\boldsymbol{F}_o}\mu_{\boldsymbol{F}_r} + C_1)(2\sigma_{\boldsymbol{F}_o\boldsymbol{F}_r} + C_2)}{\left(\mu_{\boldsymbol{F}_o}^2 + \mu_{\boldsymbol{F}_r}^2 + C_1\right)\left(\sigma_{\boldsymbol{F}_o}^2 + \sigma_{\boldsymbol{F}_r}^2 + C_2\right)}, \tag{25}$$

where $\mu_{\boldsymbol{F}_o}$ is the average value of $\boldsymbol{F}_o$, $\mu_{\boldsymbol{F}_r}$ is the average value of $\boldsymbol{F}_r$, $\sigma_{\boldsymbol{F}_o}^2$ is the variance of $\boldsymbol{F}_o$, $\sigma_{\boldsymbol{F}_r}^2$ is the variance of $\boldsymbol{F}_r$, $\sigma_{\boldsymbol{F}_o\boldsymbol{F}_r}$ is the covariance of $\boldsymbol{F}_o$ and $\boldsymbol{F}_r$, and $C_1 = (K_1 L)^2$, $C_2 = (K_2 L)^2$, K_1 and K_2 are two constants far less than 1. In this paper, the values of K_1 and K_2 are set to $K_1 = 0.01$ and $K_2 = 0.03$.

Example 1. *In this experiment, we test our method on DS1. Figure 8 shows the various band images synthesized by the nine selected elements (because there are too many bands, bands 56 and 57 are selected for display with a sampling rate of 10%; bands 66 and 67 are selected for display with a sampling rate of 20%; bands 73 and 74 are selected for display with a sampling rate of 30%; and in other examples, only two bands are displayed, but the selected bands are different); also shown are the reconstruction results of HaLRTC, TNN, LogDet-TC, Laplace-TC and the proposed tensor completion method at various sampling rates, difference images and grayscale histograms of the difference images (which are used to indicate the distribution of the specific grayscale deviation of the difference image, where the x-coordinate represents the difference between the reconstructed image and the original image, and the y-coordinate represents the number of pixels corresponding to a certain difference value. The x-coordinate and y-coordinate representations of the histograms in the experimental results of Example 2 to Example 5 have the same meaning as the histograms in Figure 8). As seen from the histograms, in the tensor completion results of the proposed method, the difference value of more pixels falls within a small range near 0. Therefore, the proposed method can obtain good tensor completion results. Compared with the images generated by other methods, the images obtained by our method have clearer boundaries and more details of the HSI.*

Example 2. *In this example, the proposed method is tested on DS2. To state the preponderance of the proposed method, the results of five methods with sampling ratios of 0.1 to 0.2 and 0.3 are given in Figure 9, which indicates that the visual effect of our method is much better than the visual effects of the completion results of the HaLRTC and TNN methods. Moreover, upon numerically quantifying the tensor completion results, the proposed method exhibits certain advantages over the LogDet-TC and Laplace-TC methods. Figure 9 ultimately demonstrates that the images obtained with our method visually appear most similar to the real HSI.*

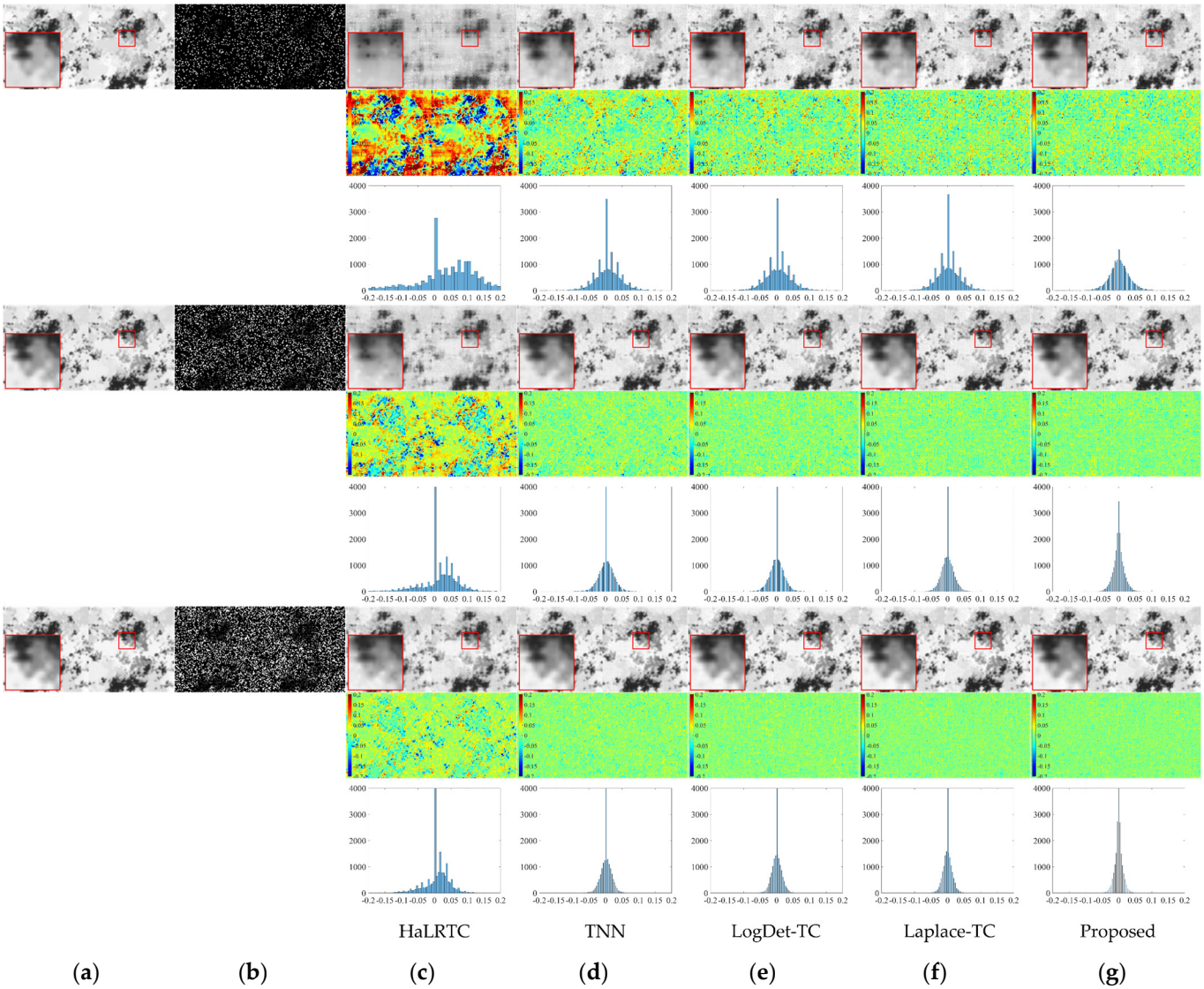

Figure 8. Tensor completion method test results on simulation dataset DS1. One area of interest (red frame) is enlarged for detailed comparison. (**a**) The original images of different bands of DS1 with different sampling ratios (because there are too many bands, bands 56 and 57 are selected for display when the sampling rate is 10% (first row); bands 66 and 67 are selected for display when the sampling rate is 20% (fourth row); and bands 73 and 74 are displayed when the sampling rate is 30% (seventh row)). (**b**) The sampling data images of the original images. From the sampling data images, the characteristic information of the retained pixels after random sampling of the specific bands can be seen. (**c**–**g**) are (in order) the tensor reconstruction results with sampling rates of 10%, 20% and 30% by HaLRTC, TNN, LogDet-TC, Laplace-TC and the proposed method. The first, fourth and seventh rows are the reconstruction results with sampling rates of 10%, 20% and 30%, respectively. The second, fifth and eighth rows show the difference images between the original image and the reconstruction results by HaLRTC, TNN, LogDet-TC, Laplace-TC and the proposed method with various sampling rates. The third, sixth and ninth rows are gray distribution histograms of the corresponding difference images.

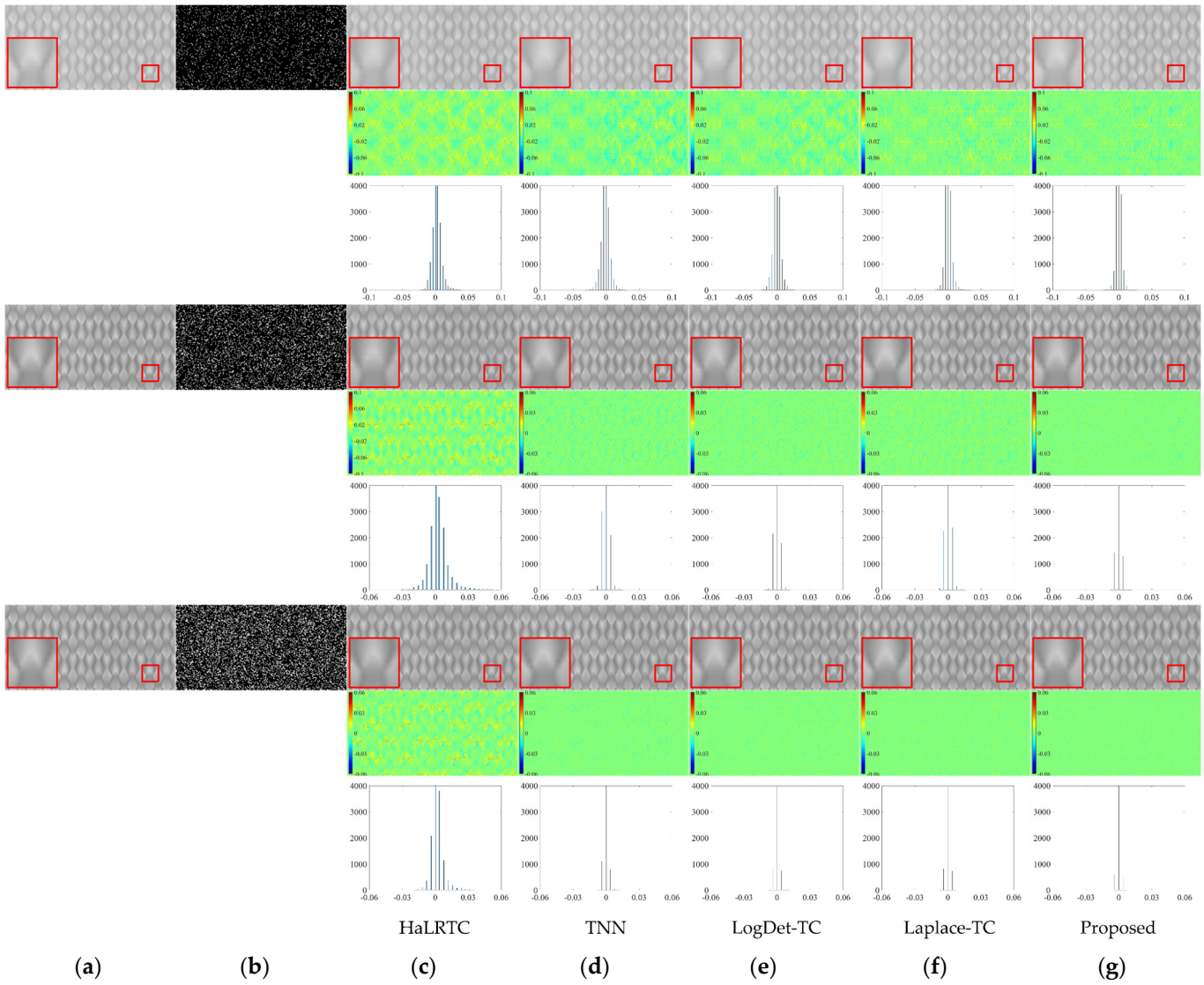

Figure 9. Test results of the tensor completion method on simulation dataset DS2. One area of interest (red frame) is enlarged for detailed comparison. (**a**) The original images of different bands of DS2 with different sampling ratios (bands 56 and 57 are selected for display when the sampling rate is 10% (first row); bands 92 and 94 are selected for display when the sampling rate is 20% (fourth row); bands 93 and 95 are selected for display when the sampling rate is 30% (seventh row). (**b**) The sampling data images of the original images with sampling rates of 10%, 20% and 30%, respectively. (**c**–**g**) are the tensor reconstruction results of HaLRTC, TNN, LogDet-TC, Laplace-TC and the proposed method. The first, fourth and seventh rows are the reconstruction results for sampling rates of 10%, 20% and 30%. The second, fifth and eighth rows show the difference images between the original image and the reconstruction results by HaLRTC, TNN, LogDet-TC, Laplace-TC and the proposed method with various sampling rates. The third, sixth and ninth rows are the gray distribution histograms of the corresponding difference images.

Example 3. *In this example, this study applies the proposed method to DS3. The results of different methods with sampling ratios of 0.1, 0.2 and 0.3 are also given in Figure 10. As we expected, the tensor completion results of our method are better than those of HaLRTC, TNN, LogDet-TC and Laplace-TC.*

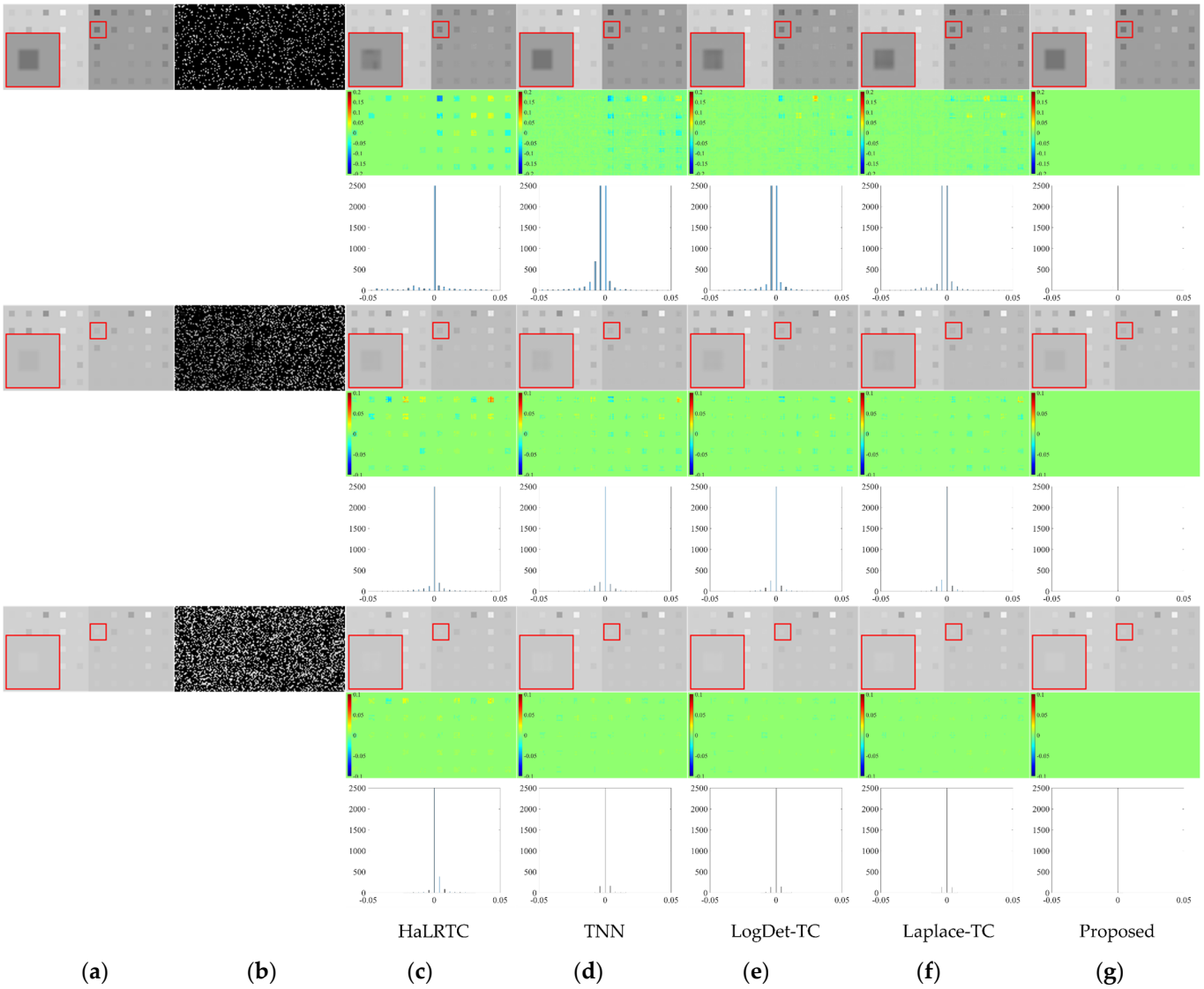

Figure 10. Tensor completion method test results on DS3. One area of interest (red frame) is enlarged for detailed comparison. (**a**) The original images of different bands of DS3 with different sampling ratios (bands 32 and 99 are selected for display when the sampling rate is 10% (first row); bands 5 and 18 are selected for display when the sampling rate is 20% (fourth row); bands 42 and 51 are selected for display when the sampling rate is 30% (seventh row). (**b**) The sampling data images of the original images with sampling rates of 10%, 20% and 30%, respectively. (**c**–**g**) are (in order) the tensor reconstruction results of HaLRTC, TNN, LogDet-TC, Laplace-TC and the proposed method for sampling rates of 10%, 20% and 30%. The first, fourth and seventh rows are the reconstruction results for sampling rates of 10%, 20% and 30%. The second, fifth and eighth rows show the difference images between the original image and the reconstruction results by HaLRTC, TNN, LogDet-TC, Laplace-TC and the proposed method with various sampling rates. The third, sixth and ninth rows are the gray distribution histograms of the corresponding difference images.

Example 4. *This example further validates the effectiveness of the proposed tensor completion method through a distribution map of ground object types from the Remote Sensing Imaging Processing Center of the National University of Singapore (Figure 11). Figure 11 shows the distribution map of ground object types in this example, which is HSI data obtained by combining 10 pure end members. Table 2 lists the ground object types and their colors, the specific composition end members and the ratios of the various end members. Dark brown represents pure water, which is composed of end member 1 and end member 10 in a ratio of 6:4. Fuchsia represents forest, which is*

composed of end member 2 and end member 7 in a ratio of 9:1. Yellow-green represents shrub, which is composed of end member 3 and end member 8 in a 1:1 ratio. Light blue indicates that the grass is directly generated by end member 4. Dark gray represents soil and man-made buildings, and is composed of end member 5 and end member 9 in a ratio of 7:3. Navy blue represents turbid water, soil and man-made buildings, and is composed of end member 6, end member 9 and end member 5 in a ratio of 4:3:3. Light blue-green represents soil and man-made buildings, generated by end member 5 and end member 9 in a 1:1 ratio. Dark blue-green represents soil and man-made buildings, generated by end member 5 and end member 9 in a ratio of 4:6.

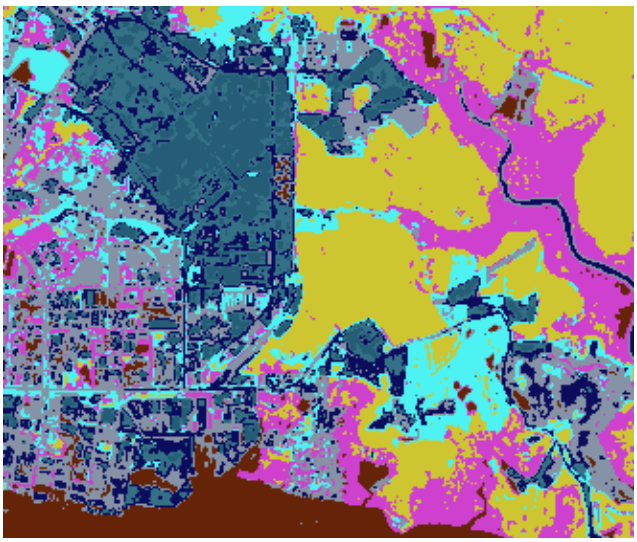

Figure 11. Distribution map of the ground object types in example 4.

Table 2. Ground object types, their colors and composition end members.

Ground Object Type Number (Color)	Ground Object Type	Composition End Members (%)
1 (Dark brown)	Pure water	End member 1 (60), end member 10 (40)
2 (Fuchsia)	Forest	End member 2 (90), end member 7 (10)
3 (Yellow-green)	Shrub	End member 3 (50), end member 8 (50)
4 (Light blue)	Grass	End member 4 (100)
5 (Dark gray)	Soil, man-made buildings	End member 5 (70), end member 9 (30)
6 (Navy blue)	Turbid water, soil, man-made buildings	End member 6 (40), end member 9 (30), end member 5 (30)
7 (Light blue-green)	Soil, man-made buildings	End member 5 (50), end member 9 (50)
8 (Dark blue-green)	Soil, man-made buildings	End member 5 (40), end member 9 (60)

Figure 12 shows the original images of different bands of HSI data (simulation dataset 4) in Figure 11, the sampling data images of the original images with sampling rates of 10%, 20% and 30%, respectively, as well as the tensor completion results obtained by HaLRTC, TNN, LogDet-TC, Laplace-TC and the proposed method. Figure 12 indicates that the difference between the real image and the result generated by the proposed method is the smallest, and the gray histogram shows that the difference in the pixel value of the proposed method decreases as the sampling rate increases. As expected, the proposed method outperforms the other methods.

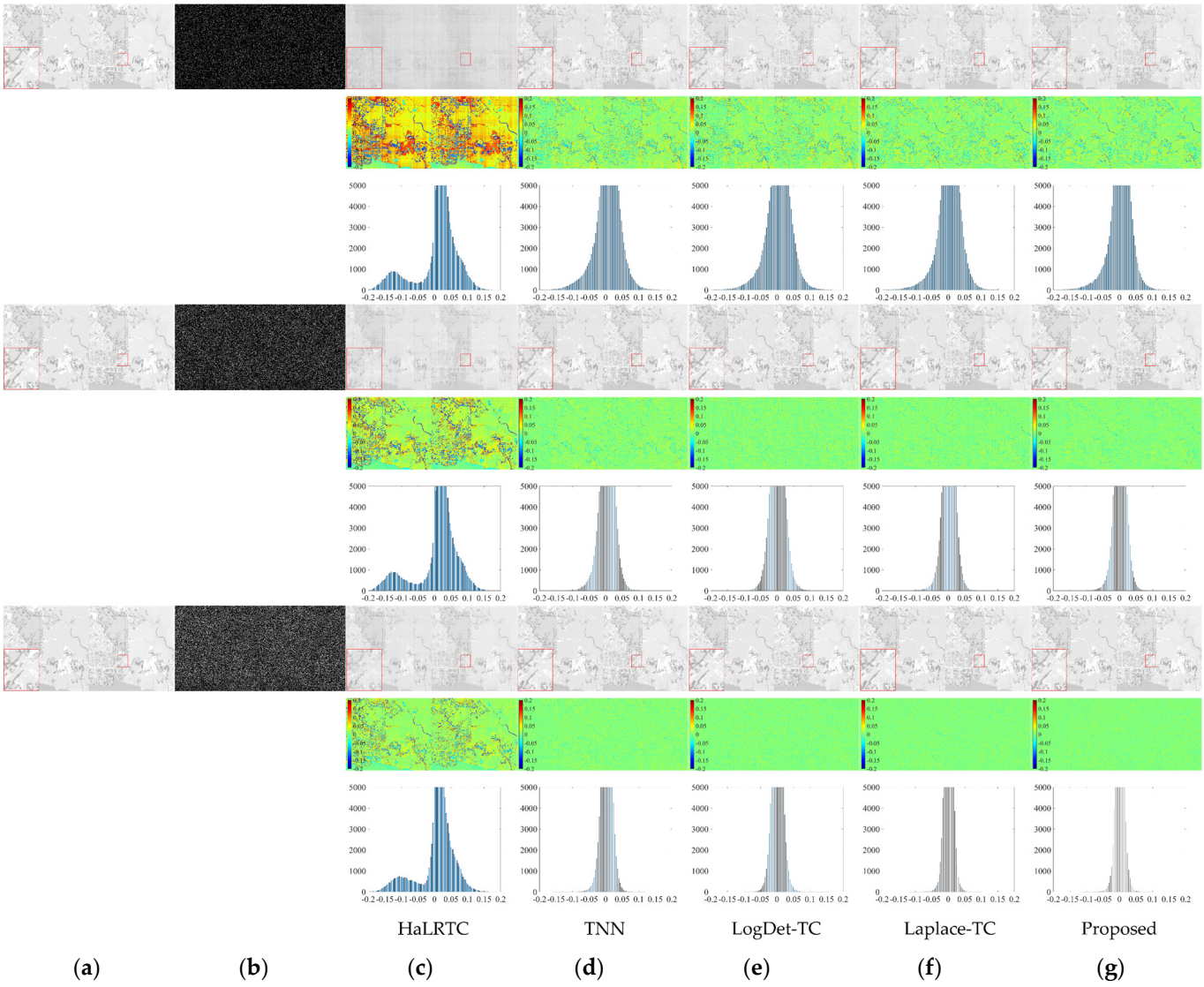

Figure 12. Tensor completion method test results on the distribution map of ground object types from the Remote Sensing Imaging Processing Center of the National University of Singapore. (**a**) The original images of different bands of simulation dataset 4 with different sampling ratios (bands 22 and 23 are selected for display at sampling rates of 10%, 20% and 30% (first, fourth and seventh rows, respectively)). (**b**) The sampling data images of the original images with sampling rates of 10%, 20% and 30%, respectively. (**c**–**g**) are the tensor reconstruction results for sampling rates of 10%, 20% and 30% by HaLRTC, TNN, LogDet-TC, Laplace-TC and the proposed method. The first, fourth and seventh rows are the reconstruction results for sampling rates of 10%, 20% and 30%. The second, fifth and eighth rows show the difference images between the original image and the reconstruction results by HaLRTC, TNN, LogDet-TC, Laplace-TC and the proposed method with various sampling rates. The third, sixth and ninth rows are the gray distribution histograms of the corresponding difference images.

Example 5. *Next, the preponderance of the proposed method is validated on the famous AVIRIS Cuprite dataset [45], which is a mineral map drawn by the U.S. Geological Survey in 1995 and contains 224 spectral bands, ranging from 0.4–2.5 µm. The experiment uses a data subset of 122,500 pixels, and the spectral bands are reduced to 188 after removing the water absorption band and data with a low signal-to-noise ratio. Figure 13 shows the tensor completion results using HaLRTC, TNN, LogDet-TC, Laplace-TC and the proposed method, all of which produce similar images. The tensor completion result obtained by the proposed method shows good spatial consistency.*

Compared with the results provided by HaLRTC and TNN, LogDet-TC and Laplace-TC have fewer outliers because they consider the spatial information between pixels. The proposed method achieves better tensor completion results than LogDet-TC and Laplace-TC, and the corresponding results usually exhibit stronger spatial consistency. Figure 13 ultimately indicates that the reconstruction result of our method is very close to the real hyperspectral image.

In conclusion, our model shows good performance in all experiments and is superior to other models. Although the speed of the proposed model is slower than that of HaLRTC, it achieves a higher tensor completion image accuracy.

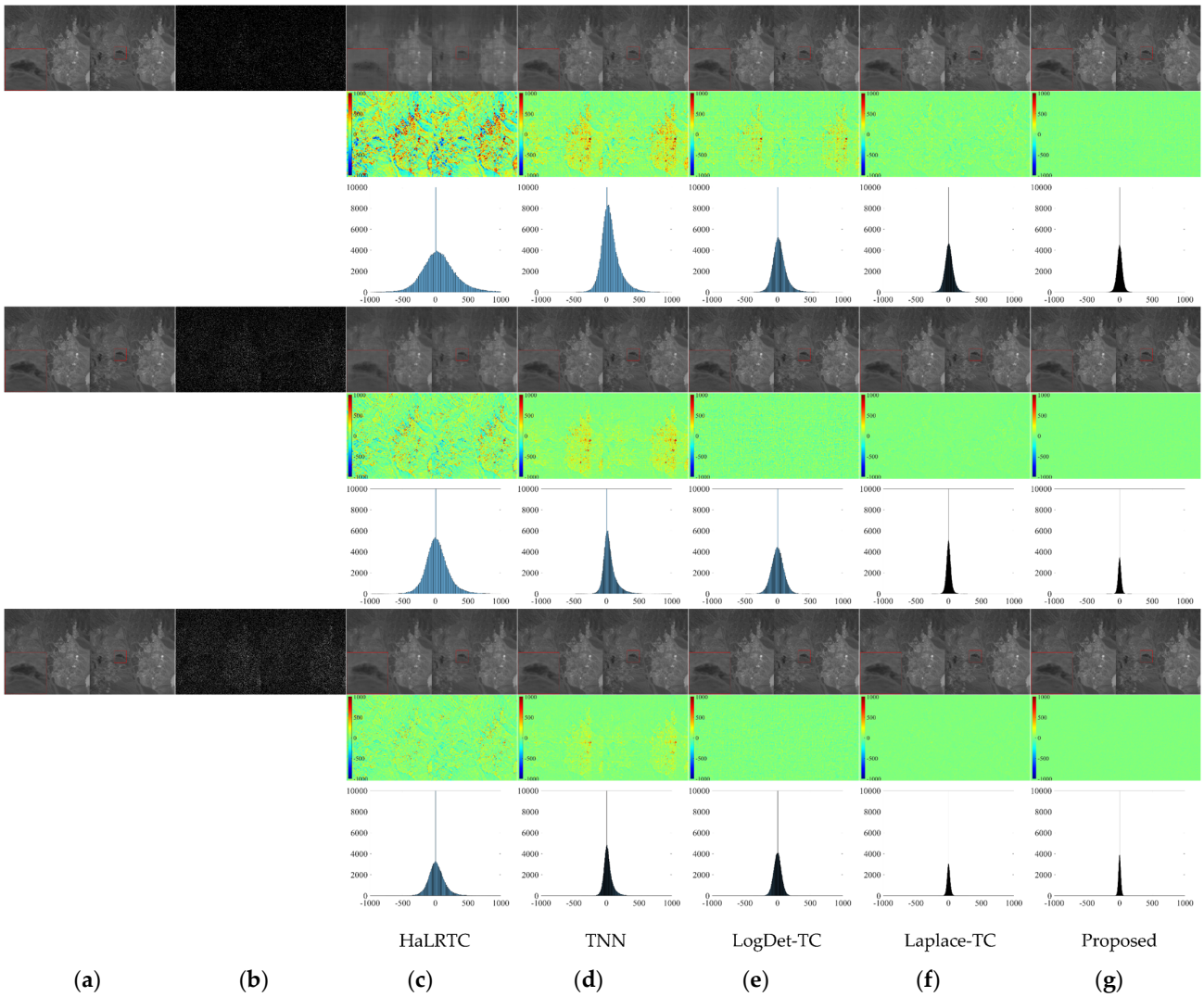

Figure 13. The results on the AVIRIS cuprite dataset. (**a**) The original images of different bands of the AVIRIS cuprite dataset with different sampling ratios (bands 72 and 74 are selected for display when the sampling rate is 10% (first row); bands 67 and 68 are selected for display when the sampling rate is 20% (fourth row); bands 65 and 68 are selected for display when the sampling rate is 30% (seventh row). (**b**) The sampling data images of the original images with sampling rates of 10%, 20% and 30%, respectively. (**c**–**g**) are the tensor reconstruction results for sampling rates of 10%, 20% and 30% by HaLRTC, TNN, LogDet-TC, Laplace-TC and the proposed method. The first, fourth and seventh rows are the reconstruction results for sampling rates of 10%, 20% and 30%. The second, fifth and eighth rows show the difference images between the original image and the reconstruction results by HaLRTC, TNN, LogDet-TC, Laplace-TC and the proposed method with various sampling rates. The third, sixth and ninth rows are the gray distribution histograms of the corresponding difference images.

To quantitatively assess the preponderance of the proposed model, the PSNR and SSIM values of various tensor completion models are listed in Table 3 for sampling ratios of 0.1, 0.2 and 0.3. Table 3 indicates that in most cases, the PSNR and SSIM values of the proposed tensor completion model are the largest. This indicates that the completion results obtained by the proposed model are the closest to the real situation. Furthermore, Table 4 shows the distribution ranges of the difference between the real image and the hyperspectral tensor completion results by the HaLRTC, TNN, LogDet-TC, Laplace-TC and proposed model under different sampling ratios. In Table 4, we set a small difference range of pixel values to evaluate various methods. The higher the percentage of pixels falling within the difference range, the smaller the difference between the original image and the recovered images, and the better the corresponding method. From Table 4, it can be seen that the proposed model has the smallest difference on different datasets. The above two points show that the SRF nonconvex low-rank regularization method can effectively improve the tensor completion result, and the proposed tensor completion model outperforms HaLRTC, TNN, LogDet-TC and Laplace-TC. In addition, the number of iterations and running time of different methods are listed in Table 5. From Tables 3–5, it can be seen that the running time of HaLRTC is the shortest, but its performance is the worst. The proposed method has the best performance and the second shortest runtime. In conclusion, our model shows good performance in all experiments and is superior to other models. Although the speed of the proposed model is slower than that of HaLRTC, it achieves a higher tensor completion image accuracy.

Table 3. The PSNR and SSIM values of the five methods.

Dataset	Sampling Rate	HaLRTC		TNN		LogDet-TC		Laplace-TC		Proposed	
		PSNR	SSIM	PSNR	SSIM	PSNR	SSIM	PSNR	SSIM	PSNR	SSIM
DS1	10%	19.1810	0.5427	26.1529	0.7779	26.5367	0.7730	27.1079	0.7811	27.6988	0.8027
	20%	24.3083	0.7850	30.4836	0.8771	31.3059	0.8830	31.9637	0.8908	32.3647	0.8979
	30%	28.7637	0.9037	33.8098	0.9271	34.9760	0.9347	35.3474	0.9380	35.6564	0.9409
DS2	10%	44.3918	0.9915	50.2451	0.9965	52.0375	0.9975	52.1378	0.9975	52.5568	0.9979
	20%	47.8194	0.9961	59.3216	0.9995	61.3278	0.9997	59.3125	0.9995	61.9718	0.9997
	30%	54.1652	0.9990	66.4177	0.9999	67.7105	0.9999	68.0190	0.9999	68.5685	0.9999
DS3	10%	46.8033	0.9928	47.5930	0.9897	50.5077	0.9940	50.9990	0.9943	67.4867	1.0000
	20%	50.9409	0.9974	54.7000	0.9978	57.3828	0.9986	57.0897	0.9986	95.5115	1.0000
	30%	54.4479	0.9986	61.0524	0.9994	63.5759	0.9996	63.4314	0.9996	98.4993	1.0000
Distribution map of ground object types	10%	21.5421	0.4777	27.8932	0.7478	28.0606	0.7472	28.2599	0.7715	28.5770	0.7949
	20%	24.9645	0.6679	32.2982	0.8828	33.1070	0.8808	33.1114	0.8976	33.3183	0.9038
	30%	26.8058	0.7725	35.8089	0.9394	36.4996	0.9364	36.8591	0.9475	37.0572	0.9502
AVIRIS Cuprite	10%	49.3208	0.4318	53.7352	0.7869	55.8124	0.8232	59.7162	0.8979	62.2725	0.9173
	20%	53.4043	0.7048	56.6647	0.8804	57.3858	0.8224	64.9149	0.9502	67.0668	0.9565
	30%	56.6848	0.8435	59.6989	0.9183	60.7367	0.8908	68.3113	0.9679	69.9921	0.9707

Table 4. Percentage of pixels within a small range of pixel values (centered on 0) of the difference images between the original image and the recovered images using five tensor completion methods.

Dataset	Sampling Rate	Difference Range of Pixel Value	Percentage of Pixels Occupied				
			HaLRTC	TNN	LogDet-TC	Laplace-TC	Proposed
DS1	10%	[−0.15,0.15]	86.330%	99.805%	99.870%	99.920%	99.940%
	20%	[−0.10,0.10]	92.820%	99.935%	99.965%	99.985%	99.990%
	30%	[−0.05,0.05]	85.450%	99.300%	99.775%	99.800%	99.860%
DS2	10%	[−0.01,0.01]	89.145%	90.415%	93.535%	96.225%	97.935%
	20%	[−0.07,0.07]	69.225%	98.090%	99.085%	98.875%	99.925%
	30%	[−0.05,0.05]	87.980%	99.795%	99.905%	99.975%	99.990%
DS3	10%	[−0.02,0.02]	97.013%	98.027%	98.951%	98.996%	100%
	20%	[−0.01,0.01]	97.867%	98.818%	99.093%	99.493%	100%
	30%	[−0.003,0.003]	94.347%	96.631%	97.173%	97.493%	100%

Table 4. *Cont.*

Dataset	Sampling Rate	Difference Range of Pixel Value	Percentage of Pixels Occupied				
			HaLRTC	TNN	LogDet-TC	Laplace-TC	Proposed
Distribution map of ground object types	10%	[−0.10,0.10]	80.146%	98.202%	98.367%	98.746%	98.912%
	20%	[−0.10,0.10]	90.904%	99.873%	99.957%	99.944%	99.955%
	30%	[−0.10,0.10]	94.792%	99.993%	99.997%	99.998%	99.999%
AVIRIS Cuprite	10%	[−400,400]	88.529%	97.606%	99.294%	99.971%	99.997%
	20%	[−100,100]	59.607%	80.892%	78.311%	98.905%	99.904%
	30%	[−50,50]	55.267%	71.592%	69.236%	96.605%	99.255%

Table 5. The number of iterations and running time of the five methods.

Dataset	Method	HaLRTC	TNN	LogDet-TC	Laplace-TC	Proposed
DS1	Number of iterations	240	348	207	202	196
	Time	8.80	61.54	53.24	51.44	46.75
DS2	Number of iterations	261	380	178	170	163
	Time	9.42	64.09	43.61	40.25	36.12
DS3	Number of iterations	313	374	200	186	181
	Time	6.56	36.75	26.83	23.71	22.82
Distribution map of ground object types	Number of iterations	362	365	202	194	187
	Time	121.06	634.11	548.77	526.93	510.04
AVIRIS Cuprite	Number of iterations	245	282	181	176	167
	Time	121.13	719.70	574.42	529.66	492.13

5. Discussion

The SRF treats singular values differently through adaptive weight allocation; therefore, a tensor completion model using the SRF as a substitution for the tensor rank is proposed in this paper. The low-rank regularization method can utilize tensor prior information in HSI data, and the minimization method of the nonconvex low-rank model can effectively complete the hyperspectral data. The proposed model is compared with HaLRTC, TNN, LogDet-TC and Laplace-TC on three synthetic hyperspectral images and two actual hyperspectral datasets at different sampling ratios. The results show that the proposed method is superior to HaLRTC, TNN, LogDet-TC and Laplace-TC according to a quantitative evaluation of the PSNR and SSIM, and the running time of the proposed method is shorter than that of TNN, LogDet-TC, and Laplace-TC.

Usually, the reconstruction error mainly occurs in the transition zone between different types of geological structures or different land cover. Remote sensing images require high reliability in transitional zones in order to clearly identify complex surface geological or ecological features. The experimental results show that even in such transitional regions, the results obtained by the proposed tensor completion method maintain good consistency with the original HSI.

6. Conclusions

Hyperspectral tensor completion has important social applicability in fields such as geological surveys, agriculture and intelligent transportation. Monitoring and assessment of environmental quality, intelligent management of crops, early diagnosis of diseases and optimization of intelligent transportation systems can be realized through the completion of hyperspectral tensors.

This paper proposes a new tensor rank nonconvex substitution (SRF), which reduces the deviation between substitution and the rank function and effectively utilizes spatial-spectral correlation, thereby improving the quality of tensor completion. On this basis, this paper proposes a tensor completion model based on the SRF, analyzes the convergence of the SRF, and designs an iterative solution algorithm based on the ADMM. The proposed model provides a certain theoretical basis and technical support for the practical application

of tensor completion. This paper focuses on tensor completion of HSI data. However, the nonconvex substitution method based on the SRF can be extended to image denoising and other fields. In addition, we will develop new tensor completion models and corresponding algorithms to improve the computational efficiency.

Author Contributions: Conceptualization, S.Y. and J.M.; methodology, S.Y., J.M. and G.L. (Guibing Li); software, G.L. (Gaoping Li) and J.M.; investigation, G.L. (Guibing Li); data curation, J.M. and W.J.; writing—original draft preparation, S.Y. and W.J.; writing—review and editing, S.Y. and W.J.; visualization, G.L. (Gaoping Li) and X.L.; project administration, J.M.; funding acquisition, S.Y. and J.M. All authors have read and agreed to the published version of the manuscript.

Funding: This study was supported in part by the Natural Science Foundation of Sichuan Province under Grants 2021ZYD0021 and 2022NSFSC0507, in part by the Sichuan Science and Technology Program under Grant No. 2023NSFSC0471, in part by the Chengdu Technological University Introduced Talents Research Startup Funds under Grant No. 2022RC002, and in part by the Southwest Minzu University Research Startup Funds under Grant No. RQD2021066.

Data Availability Statement: The data used in the first four examples are available through the link https://github.com/kaipuyu/data-for-tensor-completion (accessed on 20 June 2022), and the AVIRIS Cuprite dataset used in Example 5 is freely available through the link http://aviris.jpl.nasa.gov/html/aviris.freedata.html (accessed on 5 July 2022).

Conflicts of Interest: The authors declare no conflict of interest.

References

1. Wang, J.; Xia, Y.; Zhang, Y. Anomaly detection of hyperspectral image via tensor completion. *IEEE Geosci. Remote Sens. Lett.* **2020**, *18*, 1099–1103. [CrossRef]
2. Giannopoulos, M.; Tsagkatakis, G.; Tsakalides, P. On the impact of Tensor Completion in the Classification of Undersampled Hyperspectral Imagery. In Proceedings of the 26th European Signal Processing Conference (EUSIPCO), Rome, Italy, 3–7 September 2018; pp. 1975–1979. [CrossRef]
3. Geelen, B.; Tack, N.; Lambrechts, A. A compact snapshot multispectral imager with a monolithically integrated per-pixel filter mosaic. In Proceedings of the Advanced Fabrication Technologies for Micro/Nano Optics and Photonics VII, San Francisco, CA, USA, 7 March 2014; Volume 8974, pp. 80–87. [CrossRef]
4. Bioucas-Dias, J.M.; Plaza, A.; Camps-Valls, G.; Scheunders, P.; Nasrabadi, N.; Chanussot, J. Hyperspectral remote sensing data analysis and future challenges. *IEEE Geosci. Remote Sens. Mag.* **2013**, *1*, 6–36. [CrossRef]
5. Zhao, X.L.; Yang, J.H.; Ma, T.H.; Jiang, T.X.; Ng, M.K.; Huang, T.Z. Tensor completion via complementary global, local, and nonlocal priors. *IEEE Trans. Image Process.* **2021**, *31*, 984–999. [CrossRef]
6. Xu, T.; Huang, T.Z.; Deng, L.J.; Yokoya, N. An iterative regularization method based on tensor subspace representation for hyperspectral image super-resolution. *IEEE Trans. Geosci. Remote Sens.* **2022**, *60*, 1–16. [CrossRef]
7. Liu, J.; Musialski, P.; Wonka, P.; Ye, J. Tensor completion for estimating missing values in visual data. *IEEE Trans. Pattern Anal. Mach. Intell.* **2012**, *35*, 208–220. [CrossRef] [PubMed]
8. Lu, C.; Feng, J.; Chen, Y.; Liu, W.; Lin, Z.; Yan, S. Tensor robust principal component analysis: Exact recovery of corrupted low-rank tensors via convex optimization. In Proceedings of the IEEE Conference on Computer Vision and Pattern Recognition (CVPR), Las Vegas, NV, USA, 26 June–1 July 2016; pp. 5249–5257. [CrossRef]
9. Xie, Y.; Tao, D.; Zhang, W.; Liu, Y.; Zhang, L.; Qu, Y. On unifying multi-view self-representations for clustering by tensor multi-rank minimization. *Int. J. Comput. Vis.* **2018**, *126*, 1157–1179. [CrossRef]
10. Xie, Y.; Liu, J.; Qu, Y.; Tao, D.; Zhang, W.; Dai, L.; Ma, L. Robust kernelized multiview self-representation for subspace clustering. *IEEE Trans. Neural Netw. Learn. Syst.* **2020**, *32*, 868–881. [CrossRef]
11. Xue, J.; Zhao, Y.; Liao, W.; Chan, J.C.-W. Nonlocal low-rank regularized tensor decomposition for hyperspectral image denoising. *IEEE Trans. Geosci. Remote Sens.* **2019**, *57*, 5174–5189. [CrossRef]
12. Wu, Z.C.; Huang, T.Z.; Deng, L.J.; Huang, J.; Chanussot, J.; Vivone, G. LRTCFPan: Low-rank tensor completion based framework for pansharpening. *IEEE Trans. Image Process.* **2023**, *32*, 1640–1655. [CrossRef]
13. Xue, J.; Zhao, Y.; Liao, W.; Chan, J.C.-W. Nonlocal tensor sparse representation and low-rank regularization for hyperspectral image compressive sensing reconstruction. *Remote Sens.* **2019**, *11*, 193. [CrossRef]
14. Ran, R.; Deng, L.J.; Jiang, T.X.; Hu, J.F.; Chanussot, J.; Vivone, G. GuidedNet: A general CNN fusion framework via high-resolution guidance for hyperspectral image super-resolution. *IEEE Trans. Cybern.* **2023**, *53*, 4148–4161. [CrossRef] [PubMed]
15. Xue, J.; Zhao, Y.; Liao, W.; Chan, J.C.-W.; Kong, S.G. Enhanced sparsity prior model for low-rank tensor completion. *IEEE Trans. Neural Netw. Learn. Syst.* **2019**, *31*, 4567–4581. [CrossRef]

16. Luo, Y.S.; Zhao, X.L.; Jiang, T.X.; Chang, Y.; Ng, M.K.; Li, C. Self-supervised nonlinear transform-based tensor nuclear norm for multi-dimensional image recovery. *IEEE Trans. Image Process.* **2022**, *31*, 3793–3808. [CrossRef] [PubMed]
17. Liu, C.; Shan, H.; Chen, C. Tensor p-shrinkage nuclear norm for low-rank tensor completion. *Neurocomputing* **2020**, *387*, 255–267. [CrossRef]
18. Kilmer, M.E.; Martin, C.D. Factorization strategies for third-order tensors. *Linear Algebra Its Appl.* **2011**, *435*, 641–658. [CrossRef]
19. Semerci, O.; Hao, N.; Kilmer, M.E.; Miller, E.L. Tensor-based formulation and nuclear norm regularization for multienergy computed tomography. *IEEE Trans. Image Process.* **2014**, *23*, 1678–1693. [CrossRef]
20. Zhang, Z.; Ely, G.; Aeron, S.; Hao, N.; Kilmer, M. Novel methods for multilinear data completion and de-noising based on tensor-SVD. In Proceedings of the IEEE Conference on Computer Vision and Pattern Recognition (CVPR), Columbus, OH, USA, 24–27 June 2014; pp. 3842–3849. [CrossRef]
21. Wu, Z.C.; Huang, T.Z.; Deng, L.J.; Dou, H.X.; Meng, D. Tensor wheel decomposition and its tensor completion application. In Proceedings of the 36th Conference on Neural Information Processing Systems (NeurIPS2022), New Orleans, LA, USA, 28 November–9 December 2022; pp. 27008–27020.
22. Ji, T.Y.; Huang, T.Z.; Zhao, X.L.; Ma, T.H.; Deng, L.J. A non-convex tensor rank approximation for tensor completion. *Appl. Math. Model.* **2017**, *48*, 410–422. [CrossRef]
23. Zhang, X.; Ma, J.; Yu, S. Nonconvex Tensor Completion for 5-D Seismic Data Reconstruction. *IEEE Trans. Geosci. Remote Sens.* **2023**, *61*, 1–12. [CrossRef]
24. Xu, W.H.; Zhao, X.L.; Ji, T.Y.; Miao, J.Q.; Ma, T.H.; Wang, S.; Huang, T.Z. Laplace function based nonconvex surrogate for low-rank tensor completion. *Signal Process. Image Commun.* **2019**, *73*, 62–69. [CrossRef]
25. Zhang, X. A nonconvex relaxation approach to low-rank tensor completion. *IEEE Trans. Neural Netw. Learn. Syst.* **2018**, *30*, 1659–1671. [CrossRef]
26. Xue, S.; Qiu, W.; Liu, F.; Jin, X. Low-rank tensor completion by truncated nuclear norm regularization. In Proceedings of the 24th International Conference on Pattern Recognition (ICPR), Beijing, China, 20–24 August 2018; pp. 2600–2605. [CrossRef]
27. Chen, X.; Li, J.; Song, Y.; Li, F.; Chen, J.; Yang, K. Low-rank tensor completion for image and video recovery via capped nuclear norm. *IEEE Access* **2019**, *7*, 112142–112153. [CrossRef]
28. Lin, Z.; Xu, C.; Zha, H. Robust matrix factorization by majorization minimization. *IEEE Trans. Pattern Anal. Mach. Intell.* **2017**, *40*, 208–220. [CrossRef] [PubMed]
29. Liu, H.; Li, H.; Wu, Z.; Wei, Z. Hyperspectral image recovery using non-convex low-rank tensor approximation. *Remote Sens.* **2020**, *12*, 2264. [CrossRef]
30. Yang, Y.; Han, L.; Liu, Y.; Zhu, J.; Yan, H. A Novel Regularized Model for Third-Order Tensor Completion. *IEEE Trans. Signal Process.* **2021**, *69*, 3473–3483. [CrossRef]
31. Zhao, X.; Bai, M.; Sun, D.; Zheng, L. Robust tensor completion: Equivalent surrogates, error bounds, and algorithms. *SIAM J. Imaging Sci.* **2022**, *15*, 625–669. [CrossRef]
32. Boyd, S.; Parikh, N.; Chu, E.; Peleato, B.; Eckstein, J. Distributed optimization and statistical learning via the alternating direction method of multipliers. *Found. Trends®Mach. Learn.* **2011**, *3*, 1–122. [CrossRef]
33. Kilmer, M.E.; Braman, K.; Hao, N.; Hoover, R.C. Third-order tensors as operators on matrices: A theoretical and computational framework with applications in imaging. *SIAM J. Matrix Anal. Appl.* **2013**, *34*, 148–172. [CrossRef]
34. Du, S.; Xiao, Q.; Shi, Y.; Cucchiara, R.; Ma, Y. Unifying tensor factorization and tensor nuclear norm approaches for low-rank tensor completion. *Neurocomputing* **2021**, *458*, 204–218. [CrossRef]
35. Cai, C.; Poor, H.V.; Chen, Y. Uncertainty quantification for nonconvex tensor completion: Confidence intervals, heteroscedasticity and optimality. In Proceedings of the 37th International Conference on Machine Learning (ICML), Vienna, Austria, 12–18 July 2020; pp. 1271–1282. [CrossRef]
36. Yang, J.; Zhu, Y.; Li, K.; Yang, J.; Hou, C. Tensor completion from structurally-missing entries by low-tt-rankness and fiber-wise sparsity. *IEEE J. Sel. Top. Signal Process.* **2018**, *12*, 1420–1434. [CrossRef]
37. Kolda, T.G.; Bader, B.W. Tensor decompositions and applications. *SIAM Rev.* **2009**, *51*, 455–500. [CrossRef]
38. Gandy, S.; Recht, B.; Yamada, I. Tensor completion and low-n-rank tensor recovery via convex optimization. *Inverse Probl.* **2011**, *27*, 025010. [CrossRef]
39. Hillar, C.J.; Lim, L.H. Most tensor problems are NP-hard. *J. ACM* **2013**, *60*, 45. [CrossRef]
40. Fan, Y.R.; Huang, T.Z.; Liu, J.; Zhao, X.L. Compressive sensing via nonlocal smoothed rank function. *PLoS ONE* **2016**, *11*, e0162041. [CrossRef] [PubMed]
41. Gu, S.; Zhang, L.; Zuo, W.; Feng, X. Weighted nuclear norm minimization with application to image denoising. In Proceedings of the IEEE Conference on Computer Vision and Pattern Recognition (CVPR), Columbus, OH, USA, 23–28 June 2014; pp. 2862–2869. [CrossRef]
42. Chen, Y.; Guo, Y.; Wang, Y.; Wang, D.; Peng, C.; He, G. Denoising of hyperspectral images using nonconvex low rank matrix approximation. *IEEE Trans. Geosci. Remote Sens.* **2017**, *55*, 5366–5380. [CrossRef]
43. Abercromby, K. Communication of the NASA JSC Spacecraft Materials Spectral Database. 2006. Available online: https://www.nasa.gov/open/data.html (accessed on 3 March 2022).

44. Clark, R.; Swayze, G.; Wise, R.; Livo, E.; Hoefen, T.; Kokaly, R.; Sutley, S. *USGS Digital Spectral Library Splib06a*; Digital Data Series 231; USGS: Denver, CO, USA, 2007.
45. Han, H.; Wang, G.; Wang, M.; Miao, J.; Guo, S.; Chen, L.; Guo, K. Hyperspectral unmixing via nonconvex sparse and low-rank constraint. *IEEE J. Sel. Top. Appl. Earth Obs. Remote Sens.* **2020**, *13*, 5704–5718. [CrossRef]